2020-12-15

Hydrodynamics of onshore oscillating water column devices: A numerical study using smoothed particle hydrodynamics

Zhu, G

10.1016/j.oceaneng.2020.108226
Ocean Engineering
Elsevier

Title:
Hydrodynamics of onshore oscillating water column devices: A numerical study using smoothed particle hydrodynamics

Journal:
Ocean Engineering

Author names and affiliations:
Guixun Zhu, David Graham, Siming Zheng*, Jason Hughes, Deborah Greaves

School of Engineering, Computing and Mathematics, University of Plymouth, Drake Circus, Plymouth PL4 8AA, United Kingdom

* Email address for correspondence: siming.zheng@plymouth.ac.uk

doi:10.1016/j.oceaneng.2020.108226

Received 15 May 2020;
Received in revised form 9 October 2020;
Accepted 11 October 2020

Hydrodynamics of onshore Oscillating Water Column devices: A numerical study using Smoothed Particle Hydrodynamics

Guixun Zhu[a], David Graham[a], Siming Zheng[a,*], Jason Hughes[a], Deborah Greaves[a]

[a]*School of Engineering, Computing and Mathematics, University of Plymouth, Drake Circus, Plymouth PL4 8AA, UK*

Abstract

Oscillating water column (OWC) device is possibly the most studied among various wave energy converters and many different realisations of the technology have been investigated. To study the complex hydrodynamic behaviour of an OWC, a two-dimensional numerical wave tank based on the weakly compressible smoothed particle hydrodynamics (SPH) method is developed in this paper. A simplified pneumatic model is proposed here to simulate the effect induced by a pneumatic power take-off system within the framework of a single-phase SPH model, and implemented to determine the air pressure imposed on the free surface inside the OWC chamber. Additionally, a regional ghost particle approach, as boundary condition in SPH, is proposed to better simulate fluid dynamics near a thin wall. The overall computation cost is reduced dramatically due to the employment of the regional ghost particle boundary condition method. First, the numerical model is validated under regular waves using published physical and numerical data. An extensive campaign of computational tests is then carried out, studying the performance of the OWC for various wall thicknesses and damping coefficient under various wave conditions. The results demonstrate that the present SPH model can be used as a practical tool for the development of high-performance OWCs.

*Corresponding author. Email: siming.zheng@plymouth.ac.uk

(https://doi.org/10.1016/j.oceaneng.2020.108226)

Keywords: wave power, oscillating water column, Smoothed Particle Hydrodynamics (SPH), power take–off system, thin wall

1. Introduction

Powered by the increasing demand for energy and to the uncertainty of climate change, marine renewable energies are among the high priority research issues. As one of the most available ocean energy sources, wave energy has the advantage of relatively high energy density and limited negative environmental impact in use (Drew et al., 2009). A large number of wave energy converters (WECs) have been developed so far, of which Oscillating Water Column (OWC) may be regarded as one of the most successful types of WEC, and has attained the stage of deploying full–scale prototypes (Falcão and Henriques, 2016). A classic OWC consists of a water column and an overlying thin–walled air chamber with its bottom/sidewall submerged and partially open to the sea (Falcão and Henriques, 2016). The opening allows the water column to oscillate up and down driven by the incident waves. The motion of the water column, in turn, drives the air trapped in the chamber to pass through an air turbine, which is usually placed in a duct on the top of the structure. Ultimately, electricity is produced by a generator connected to the turbine.

Many potential flow theory based theoretical models have been proposed for studying the hydrodynamic performance of OWCs. Evans (1978) developed a theoretical model of a fixed OWC device by considering the chamber free surface movement as a rigid weightless piston. This theory can be applied when the width of the inside free surface is small compared to the wavelength. Considering the linear and nonlinear power take–off (PTO) system, Sarmento and Falcão (1985) found that the maximum efficiency of a 2D OWC device with nonlinear PTO was only slightly lower than that achieved in the linear case. In their model, the immersed wall of the air chamber was assumed to have a shallow draught unless it was a submerged vertical reflecting wall, i.e., the wave diffrac-

tion due to the immersed part was ignored except for the wave reflection by a bottom–mounted vertical wall behind the chamber. Later, Evans and Porter (1995) developed a more general model for a near–shore OWC with both the internal pressure distribution and the effect of a finite draught of chamber wall considered. Auxiliary functions expanded in Chebychev polynomials were introduced to approximate the singular behaviour of the fluid motion at the salient corner. It was revealed that the peak of the frequency response of wave power absorption efficiency moved towards low wave frequencies with the increase of the immersion of the front–wall. Their model was recently extended by He et al. (2019a) to study wave power extraction and wave attenuation of a pile–supported OWC breakwater. More recently, Deng et al. (2020) proposed a novel near–shore OWC device with the front thin wall replaced by a thick freely surging lip–wall. A theoretical model, in which auxiliary functions were expanded in Gegenbauer polynomials, was also proposed to study the hydrodynamic characteristics of the device. The existence of a freely surging lip–wall was found to increase the power absorption of the device over a wide frequency bandwidth. Apart from these 2D theoretical models, 3D models were developed to study the hydrodynamic performance of vertical cylinder-shaped OWCs. Martinsrivas and Mei (2009a,b) proposed 3D models to investigate the wave interaction with a thin-walled OWC deployed along a straight coast and at the tip of a thin breakwater, respectively. A theoretical model was also developed by Zheng et al. (2019b) to study the wave power absorption of a breakwater/coast integrated OWC without the restriction of the thin-wall assumption. It was observed that the thinner the OWC chamber wall, the larger and broader the main peaks of the frequency response of wave power capture efficiency. Their model was later extended to assess the performance of multiple OWCs along a straight coast (Zheng et al., 2019a).

The theoretical models are generally limited to simulate OWCs with regular geometrical configurations, e.g., vertical thin walls or rectangular–shaped thick walls for the 2D problem. Adding to the theoretical studies, some potential flow theory–based numerical models were also developed (Ning et al., 2017; Nader

et al., 2014), which can be used to deal with hydrodynamic models of an OWC with complex structural shapes. In spite of the high computation efficiency of the potential flow theory–based theoretical/numerical models, they have obvious shortcomings in handling hydrodynamic problems with strong nonlinearity, complex viscous fluids, dispersion, wave breaking, turbulence, and vortex shedding due to the drawbacks of potential flow theory.

In comparison, the commonly used numerical wave tanks (NWTs) that solve the Navier-Stokes equations can achieve reliable results without those shortcomings in dealing with fully nonlinear hydrodynamic problems. Zhang et al. (2012) applied a two–phase level–set immersed boundary method to simulate a 2D OWC. The effect of wave condition and geometric dimensioning of the OWC was investigated. López et al. (2014) used a 2D RANS–VOF model (Star–CCM+) to study the optimum turbine–chamber coupling for OWC under regular and irregular waves. The model developed by them allows the damping condition to maximize the hydrodynamic performance to be determined. Kamath et al. (2015) employed REEF3D, an open–source CFD code, to study a 2D OWC under operational wave conditions. The rigid piston–like motion of the internal free surface was seen in the simulation with the lower wave steepness, whereas non–uniform motion was observed at the higher wave steepness. Vyzikas et al. (2017) investigated the behavior of a fixed OWC by using a 2D air–water incompressible CFD model (OpenFOAM), the numerical results of which were found to be in excellent agreement with experimental data. Moreover, an approach was proposed to estimate the OWC resonance frequency. The study of an offshore stationary asymmetric OWC device was carried out by using the OpenFOAM CFD software package by Simonetti et al. (2017, 2018). The results showed a strong mutual interaction of the PTO damping, the front wall draught and the relative OWC chamber length on the wave power absorption. More recently, a fully nonlinear numerical 3D wave tank (NWT) was developed by Elhanafi et al. (2017) and Elhanafi and Kim (2018) using the Star–CCM+ CFD code. They found that full–scale air compressibility could reduce the optimum damping at the resonant period, and the extracted pneumatic energy

significantly increased as wave height increased.

The grid–based numerical methods, although widely used in coastal and offshore engineering, may have difficulty in dealing with extreme deformation problems like strong wave breaking, splashing, and fragmentation of the air–water surface. In comparison, the meshless methods are more useful for treating strong nonlinear flows, complex fluid dynamics and the dramatic response of offshore structure in extreme wave conditions. Smoothed Particle Hydrodynamics (SPH) is one of the most popular meshless methods and has attained the required level of development to be used for engineering purposes thanks to more and more powerful computer technology (Crespo et al., 2017). Since Monaghan (1994) used SPH to study free–surface flows, it has been continuously developed and employed to solve various hydrodynamic problems. Sun et al. (2018) used the recently developed δ^+-SPH scheme to simulate both 2D and 3D entry problems. Zhang et al. (2019) used a SPH model with mixed characteristic boundary condition to simulate flows past a hydrofoil. He et al. (2020) presented a numerical investigation of the solitary wave breaking over a slope by using a finite particle method which is an enhanced SPH method. The results show that the wave dissipation reduces when wave breaking types changed from spilling breaker to surging breaker. Violeau and Rogers (2016) assessed some recent trends in the SPH method, with particular focus on free-surface flow simulations. Gotoh and Khayyer (2018) gave a review on several latest advancements related to particle methods with applications in coastal and ocean engineering. Ye et al. (2019) reviewed the recent developments of SPH in methodology and applications for modeling complex fluid flows. Liu and Zhang (2019) presented a review of the recent developments in SPH based modeling techniques for solving fluid-structure interaction-related problems.

In SPH, the substances are modelled as discrete moving particles. Therefore, SPH is a Lagrange mesh–free method, in which the free surface is naturally formed without introducing diffusive interfacial tracking algorithms. SPH is deemed to be an ideal technique to simulate complex free–surface flows and shows several advantages in simulation of wave–structure interaction (Crespo

et al., 2017): (i) The free surface can be automatically detected without the need for a special interface detection treatment. (ii) Moving complex boundaries and interfaces are easily handled by the Lagrange formulation. (iii) Multiphase flows are simulated without detecting the interface since each particle holds its material properties.

In the recent decade, the SPH method has been implemented for OWC investigations. Didier et al. (2016) tentatively studied the hydrodynamics of an onshore OWC device in a rough sea state with complicated wave breaking, impact loads and overtopping, using the SPH numerical model SPHyCE. The resonance phenomena in the OWC chamber was accurately modeled with their model. Crespo et al. (2017) applied GPU–accelerated SPH code (DualSPHysics) to simulate wave interaction with a floating offshore moored OWC device. It was demonstrated that the model was able to reproduce the water surface correctly inside the chamber with the air pressure in the chamber neglected. The hydrodynamic behaviour of an onshore OWC was also studied by Wen et al. (2018) with the employment of an improved SPH model, in which the turbulence effect was considered. The internal free surface elevations, the total forces acting on the front wall of the OWC chamber, the turbulence energy distribution, together with the sloshing phenomenon for different wave conditions were investigated. It was revealed that the sloshing phenomenon could be observed inside the OWC chamber for a smaller value of the front wall depth. Besides that, SPH method has been extended to simulate other wave energy devices. Zhang et al. (2018) applied SPH in the simulations of an oscillating wave surge converter (OWSC). The results demonstrated that the active power of land hinged OWSC strongly depends on both the PTO damping coefficients and the wave periods. Brito et al. (2020) presented a SPH model with nonlinear mechanical constraints for OWSC. They analyzed the effect of the flap inertia by changing its mass, centre of mass, height and thickness. Liu et al. (2020) adopted a SPH model to investigate a cylindrical OWSC with a flap consisting of several cylinders. Numerical results indicated that the heavier and thinner the flap, or the higher the hinge, the better the wave-absorption performance.

As the damping increased, the extracted energy was found to increase initially and then decrease. Madhi and Yeung (2018) applied the Weakly Compressible Smoothed Particle Hydrodynamics (WCSPH) to analyze the forces experienced in breaking-waves condition in order to improve the survivability of asymmetrical wave-energy converters.

It is worth mentioning that, to the best of the authors' knowledge, the air pressure fluctuations inside OWC chambers have never been modeled in any published SPH–based OWC research. Furthermore, this is the first publication including air fluxes using a pneumatic model in a single–phase SPH model. Indeed, for OWC devices, water and air are strongly coupled inside the OWC chambers, affecting the hydrodynamic performance significantly. The air pressure in the OWC chamber acts on the free internal water surface and affects the oscillation of the water column directly; meanwhile, the air pressure is strongly dependent on the water column's oscillation. Admittedly, the air–water two phase SPH model can solve this problem naturally and physically in a straightforward manner but this method incurs a computational cost (Gong et al., 2016). With the same numerical terms in SPH method, the calculation cost for single water phase model is undoubtedly less than that for air-water phase model. Motivated by the apparent lack of effective SPH models for the simulation of OWCs consisting of PTO systems, in this paper, a single–phase SPH model with a pneumatic model is proposed to study the performance of OWC devices. The air pressure is assessed based on a linear/nonlinear function of the air volume flux across the free surface inside the chamber and is instantaneously applied back to the internal free surface boundary without modelling the air phase. In addition, a regional ghost particle approach is employed to simulate the thin front wall, which provides an effective option to accelerate SPH modeling. The simulation of solid boundary condition is important for several SPH applications. One of the main problems for solid boundary simulation in SPH is the selection of kernel truncation near the boundary, which may lead to the rapid decrease of interpolation accuracy. Over the years many different approaches have been presented. A classical method is the ghost particles approach devel-

oped by Colagrossi and Landrini (2003), in which the fluid particles approaching the solid boundary are mirrored in respect to the solid. Marrone et al. (2011) proposed a fixed ghost particle approach. In their model, the ghost particles are fixed in the frame of reference of the body and the values attributed to these particles are calculated from corresponding interpolation nodes. Meringolo et al. (2015) developed a SPH model to simulate thin solid bodies using a multi-nodes fixed ghost approach. More interpolation nodes were associated to a single solid particle to overcome disadvantages of the choice of the initial spatial resolution of the model for immersed thin structure simulation. Nevertheless, the layers of ghost particles are limited in their approach when the front wall is too thin. In the present work, a regional ghost particle approach is proposed to simulate the thin front wall, which provides a more effective option to accelerate SPH modelling than the multi-node fixed ghost approach.

The remainder of this paper is organized as follows. The SPH mathematical theory, the pneumatic model and the regional ghost particle approach adopted in this study are described in §2. Validation of the present model, including wave generation and simulation of onshore OWC devices, is described in §3. The verified SPH model is applied to the study of the hydrodynamics of an onshore OWC under various conditions in §4. Finally, conclusions are drawn in §5.

2. SPH model

2.1. Governing equation

In this study, the flow is assumed to be viscous, weakly–compressible, and adiabatic. The adopted governing equations consist of the Navier–Stokes equations in the Lagrange framework and a linearized version of the equation of state

to determine the pressure describing the evolution of the flow field:

$$\begin{cases} \frac{\mathrm{d}\boldsymbol{u}}{\mathrm{d}t} = -\frac{1}{\rho}\nabla P + F_\alpha + \boldsymbol{g}, \\ \frac{\mathrm{d}\rho}{\mathrm{d}t} = -\rho\nabla\cdot\boldsymbol{u}, \\ \frac{\mathrm{d}\boldsymbol{r}}{\mathrm{d}t} = \boldsymbol{u}, \\ P = (\rho - \rho_0)c^2, \end{cases} \tag{1}$$

where ρ, ρ_0, $\boldsymbol{u}$, t, $\boldsymbol{r}$ and P denote the instant density, initial density, velocity vector, time, position vector and pressure, respectively. F_α is the viscosity term and $\boldsymbol{g}$ represents the gravitational acceleration. The pressure P is calculated directly from the density using a linear equation of state. c is the numerical speed of sound, which is chosen following an analysis presented by Morris et al. (1997) to approximate an incompressible flow accurately. In our work, the numerical speed of sound is determined by

$$c^2 \geq \max\left\{\frac{U_{max}^2}{0.01}, \frac{gH}{0.01}\right\}, \tag{2}$$

where U_{max} and H are the maximum velocity and the undisturbed fluid depth, respectively. The above formulation aims to ensure that the variation in fluid density is less than 1%.

2.2. Discrete governing equations

The governing equation can be discretized by an SPH approximation. According to the work in Liu and Liu (2010), the discrete pressure gradient can be written as:

$$-\frac{1}{\rho_i}\nabla P_i = -\frac{1}{\rho_i}\sum_j (P_j + P_i)\cdot\nabla_i W_{ij} V_j. \tag{3}$$

where $W_{ij} = W(r_i - r_j, h)$ is the kernel function, h is the smoothing length defining the influence area. Subscripts i and j denote the particle index. V_j is the volume of the particle ($V_j = m_j/\rho_j$, m denotes mass).

The artificial viscosity term can be added to the momentum equation to produce bulk and shear viscosity and also to stabilize the scheme as follows

(Monaghan, 2005)

$$F_\alpha = \sum_j \alpha hc \frac{(\boldsymbol{u}_j - \boldsymbol{u}_i)\cdot(\boldsymbol{r}_j - \boldsymbol{r}_i)}{|\boldsymbol{r}_j - \boldsymbol{r}_i|^2} \cdot \nabla_i W_{ij} V_j. \tag{4}$$

Furthermore, the relationship between the artificial viscous coefficient α and the physical kinematic viscosity υ is (Antuono et al., 2011)

$$\upsilon = \frac{\alpha hc}{2(dim+2)}, \tag{5}$$

where dim is the number of spatial dimension. To avoid using an artificial viscosity model, the viscous term is applied here:

$$F_\alpha = 2(dim+2)\cdot\upsilon \sum_j \frac{(\boldsymbol{u}_j - \boldsymbol{u}_i)\cdot(\boldsymbol{r}_j - \boldsymbol{r}_i)}{|\boldsymbol{r}_j - \boldsymbol{r}_i|^2} \cdot \nabla_i W_{ij} V_j. \tag{6}$$

The velocity divergence can be discretized in (Liu and Liu, 2010)

$$-\rho_i \nabla\cdot\boldsymbol{u}_i = -\sum_j (\boldsymbol{u}_j - \boldsymbol{u}_i)\cdot\nabla_i W_{ij} V_j, \tag{7}$$

where u_i is the velocity of particle i. Spurious numerical oscillations generally exist in the pressure and density fields for traditional weakly compressible SPH. One of the popular methods to overcome the problem is the δ–SPH model (Antuono et al., 2012), in which a diffusive term is added to the continuity equation, i.e., Eq. (7), to remove the spurious high–frequency oscillations. This method is employed in the present study with the added diffusive term expressed as

$$\delta hc \sum_j \Psi_{ij}\cdot\nabla_i W_{ij} V_j, \tag{8}$$

where $\delta = 0.1$ (Marrone et al., 2011) for all the following cases and

$$\begin{cases} \Psi_{ij} = 2(\rho_j - \rho_i)\frac{\boldsymbol{r}_j - \boldsymbol{r}_i}{|\boldsymbol{r}_j - \boldsymbol{r}_i|^2} - (\langle\nabla\rho\rangle_i^L + \langle\nabla\rho\rangle_j^L), \\ \langle\nabla\rho\rangle_i^L = \sum_j (\rho_j - \rho_i) L_i \nabla_i W_{ij} V_j, \quad \text{where} \quad L_i = \left[\sum_j (\boldsymbol{r}_j - \boldsymbol{r}_i)\otimes\nabla_i W_{ij} V_j\right]^{-1} \end{cases} \tag{9}$$

where $\otimes$ denotes tensor product. In the present simulation, a prediction–correction time–stepping scheme is applied to ensure second–order accuracy

(Monaghan, 1989). Moreover, to ensure numerical stability, the maximum time–step is chosen based on several criteria:

$$\Delta t \leq \frac{h}{c}, \tag{10}$$

the viscous diffusion condition,

$$\Delta t \leq 0.125 \frac{h^2}{v}, \tag{11}$$

and the body force condition,

$$\Delta t \leq 0.25 \sqrt{\frac{h}{g}}. \tag{12}$$

In the SPH method, the time step is subject to empirical stability criteria. The time step should be less than these three values for stability. The time steps are also updated to satisfy CFL-condition based on the maximum artificial sound speed as Eq. (10). If the flow is viscous, the efficiency of incompressible SPH can be further increased by a multi-time-step technique. Time-steps are updated according to conditions Eq. (11). Considering the effect of body force, time-steps are updated according to condition Eq. (12). To satisfy all conditions, the global time–step is taken as the minimum of Eqs. (10–12).

2.3. Pneumatic model

Hydrodynamics and aerodynamics are strongly coupled inside the chamber of an OWC. The up and down motion of the water column enclosed by the chamber moves the air inside and outside of the OWC chamber, driving the air through a turbine and generator in order to capture wave power. The variable air pressure inside the chamber is associated with the change in the air volume (i.e., the water column oscillation). The air–water two–phase model could be a straightforward way to simulate this phenomenon theoretically and naturally but requires an expensive computational cost for SPH methods. A single–phase SPH model with a pneumatic model is proposed here and found to be an effective alternative option of the expensive two–phase model.

A parabolic expression between air velocity in the duct and air pressure in the chamber, P_a, was considered (López et al., 2014; Simonetti et al., 2017):

$$P_a(t) = \begin{cases} (K_{dm} q_d(t))^2, & q_d(t) > 0, \\ -(K_{dm} q_d(t))^2, & q_d(t) \leq 0, \end{cases} \tag{13}$$

where K_{dm} is the damping coefficient and q_d is the air volume per second per unit width on the duct. $q_d(t) > 0$ denotes that air flows into the chamber. When the air volume enclosed by the chamber is small, the air compressibility can be neglected (Simonetti et al., 2018; Elhanafi et al., 2017). Thus the air velocity in the duct can be expressed in terms of the rate of change of vertical displacement of the internal free surface. Neglecting air compressibility inside the OWC chamber, the airflow rate $q_d(t)$ per unit width near the duct can be calculated as follows López et al. (2014):

$$q_d(t) = \frac{\Delta V}{w_c \Delta t}, \tag{14}$$

where ΔV denotes the volume change of air phase in the chamber at Δt (Δt=0.01 s in our work). w_c represents the width of the chamber. Since the volume of the cavity is constant, the volume change of air phase can be obtained by the evolution of the surface level. As shown in Fig. 1, the cavity is uniformly divided into $1.5h$ along the length direction. As a Lagrangian mesh-free method, it is difficult to determine the instantaneous free surface level accurately in SPH. Thanks to the obscuring effect of the front wall, the wave motion inside the chamber is not dramatic, and mostly, neither splashing nor wave rolling happens. With this information, we can obtain the volume change ΔV of air phase in the chamber.

The obtained air pressure is instantaneously imposed on the free surface particle inside the chamber. According to the work in Lee et al. (2008), the divergence of particle position $\nabla \cdot \boldsymbol{r}$ is used to detect the free surface particles $\mathcal{F}$. Generally, the criterion for $\nabla \cdot \boldsymbol{r}$ is 2.0 in previous work for 2D problems (3.0 for 3D problems). However, the irregular distribution of particles causes confusion to recognize free surface particles. The geometric method developed by Huang et al. (2018a,b) can detect the two layers of particles for the cubic

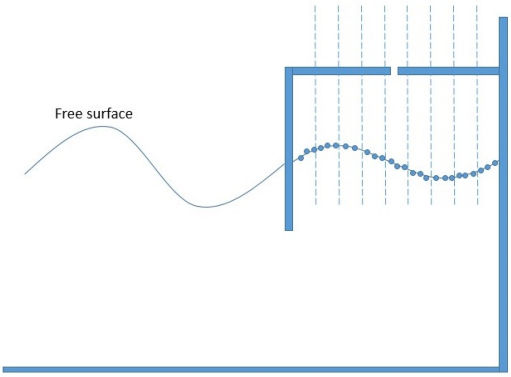

Figure 1: Sketch of the approach for determining air volume change and free surface level.

spline function and three layers of particles for the Gaussian function. In this work, the two layers of free surface particles are considered. According to wave simulation tests, if $\nabla \cdot \boldsymbol{r} \leq 1.89$, two layers of free surface particles can be captured well. The identified surface particles of a wave case at different times are shown in Fig. 2. Most surface particles at the surface are identified but not all of them, and the results show that sufficient particles are defined in order to track the interface correctly. Thus, a criterion set to 1.89 is used in present work:

$$\forall \text{ particle } i \in [\nabla \cdot \boldsymbol{r}_i = \sum_j \boldsymbol{r}_{ij} \cdot \nabla_i W_{ij} V_j \leq 1.89] \Longrightarrow \text{particle } i \in \mathcal{F}. \tag{15}$$

The change of air pressure is directly imposed on the pressure of the free surface particles inside the chamber. The pressure gradient of a free surface particle in the chamber can be rewritten as

$$-\frac{1}{\rho_i}\nabla P_i = \begin{cases} -\frac{1}{\rho_i}\sum_j \left[(P_j + P_a) + (P_i + P_a)\right] \cdot \nabla_i W_{ij} V_j, & i \in \mathcal{F} \text{ in the chamber,} \\ -\frac{1}{\rho_i}\sum_j (P_j + P_i) \cdot \nabla_i W_{ij} V_j, & \text{otherwise.} \end{cases} \tag{16}$$

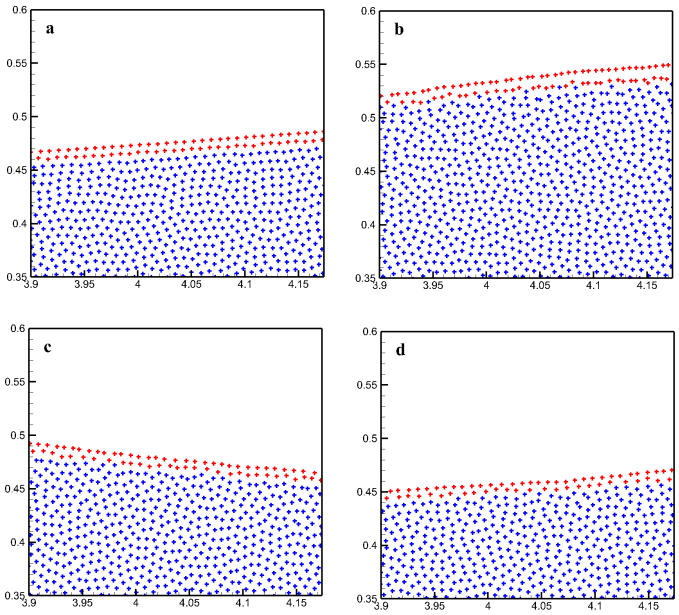

Figure 2: Examples of detecting surface particle (Wave case in Section 4.1, a: $t = 4.0$ s, b: $t = 6.0$ s, c: $t = 8.0$ s, d: $t = 10.0$ s. Red dots denote free surface particles).

Finally, the governing equation can be written as:

$$\begin{cases} \frac{\mathrm{d}\boldsymbol{u}_i}{\mathrm{d}t} = -\frac{1}{\rho}\nabla P_i + F_\alpha + \boldsymbol{g}, \\ \frac{\mathrm{d}\rho_i}{\mathrm{d}t} = -\sum_j (\boldsymbol{u}_j - \boldsymbol{u}_i)\cdot\nabla_i W_{ij} V_j + \delta hc \sum_j \Psi_{ij}\cdot\nabla_i W_{ij} V_j, \\ \frac{\mathrm{d}\boldsymbol{r}_i}{\mathrm{d}t} = \boldsymbol{u}_i, \\ P_i = (\rho_i - \rho_0)c^2. \end{cases} \tag{17}$$

2.4. Solid boundary condition

Following Marrone et al. (2011), the present model uses the regular fixed ghost particles that are created to represent the solid boundary only once at the initial time. All these fixed ghost particles have the same initial particle spacing as that of the fluid particles. Three layers of ghost particles are used as the Gauss kernel function selected with $h = 1.2 * dx0$, where $dx0$ is defined as the variable for initial particle spacing. The radius of influence $\mathcal{K}$, is then $\mathcal{K} = 3.6 * dx0$ for the Gauss kernel function. To calculate the physical property of the ghost particles, interpolation nodes are created at the position determined by mirroring the position of the fixed ghost particle into the fluid domain. The number of layers is associated with the kernel function, i.e., it is necessary to cover at least three layers of ghost particles for the Gauss kernel function (case of kernel support domain of $3h$). Each ghost particle has an interpolation node associated with it. The physical information of interpolation nodes can be obtained by using a SPH kernel interpolation of the fluid particles as follows:

$$\begin{cases} \rho_m = \frac{\sum_{j\in fluid}\rho_j V_j W_{mj}}{\sum_{j\in fluid} V_j W_{mj}}, \\ \boldsymbol{u}_m = \frac{\sum_{j\in fluid}\boldsymbol{u}_j V_j W_{mj}}{\sum_{j\in fluid} V_j W_{mj}}. \end{cases} \tag{18}$$

where ρ_m and $\boldsymbol{u}_m$ represent the density and velocity of interpolation nodes, respectively, and $j \in fluid$ denotes all the fluid particles in the support domain of interpolation node m.

The pressure is set at the fixed ghost particles to enforce the following Neumann condition:

$$\frac{\partial P}{\partial \boldsymbol{n}_w} = \rho[\boldsymbol{f}\cdot\boldsymbol{n}_w - \boldsymbol{a}_b\cdot\boldsymbol{n}_w], \tag{19}$$

where $\boldsymbol{f}$ is acceleration due to generic body force and $\boldsymbol{a}_b$ is the acceleration of the wall boundary. $\boldsymbol{n}_w$ is the normal direction of the wall. Thus, the pressure of ghost particles P_g can be calculated as

$$P_g = P_m + \frac{\partial P}{\partial \boldsymbol{n}_w} \cdot (\boldsymbol{r}_m - \boldsymbol{r}_g), \tag{20}$$

where P_g, P_m, $\boldsymbol{r}_g$ and $\boldsymbol{r}_m$ are the pressure and position of the ghost particles and the interpolation nodes, respectively, in which P_m can be obtained by the density of interpolation nodes using the equation of state. The normal $\boldsymbol{n}_w$ in the direction of the wall can be determined by a generalized and straightforward method,

$$\boldsymbol{n}_w = \frac{\sum_{j \in fluid} \nabla W_{jf} V_j}{|\sum_{j \in fluid} \nabla W_{jf} V_j|}. \tag{21}$$

For free–slip and no–slip conditions, the normal velocity of the ghost particles is reversed with the same normal velocity as the corresponding interpolation node to avoid particles crossing the solid profile and to satisfy the boundary condition $\boldsymbol{u} \cdot \boldsymbol{n}_w = \boldsymbol{u}_w \cdot \boldsymbol{n}_w$. In the free–slip case, the tangential component of velocity is maintained unaltered during the mirroring procedure, whereas, its direction in the no–slip case is reversed.

For a moving boundary (i.e., the moving wall of a wavemaker), free-slip condition is applied here. Thus, the wavemaker ghost particles have the same tangential components with interpolation nodes, $u_{\tau g} = u_{\tau m}$, where $u_{\tau g}$ is the local tangential components of the velocity associated with the fixed ghost particle, $u_{\tau m}$ is the local tangential components of the velocity evaluated on the corresponding interpolation nodes. The velocity imposed on the fixed ghost particle characterizing the wavemaker should satisfy the boundary condition $\boldsymbol{u} \cdot \boldsymbol{n}_w = \boldsymbol{u}_w \cdot \boldsymbol{n}_w$, in which $\boldsymbol{u}$ is the numerical velocity at the boundary position and $\boldsymbol{u}_w$ is the velocity of the moving wall. Hence the local normal components of the velocity associated with the ghost particles can be calculated by $u_{ng} = 2u_{nw} - u_{nm}$, where u_{ng} is the local normal components of the velocity associated with the fixed ghost particle, u_{nw} is the local normal component of the displacement velocity associated with the moving wall, and u_{nm} is the local

normal component of the velocity evaluated on the corresponding interpolation nodes.

2.4.1. Regional ghost particle approach

For a conventional fixed ghost particle boundary approach, a solid boundary should be represented by a couple of layers of ghost particles to avoid kernel truncation error and in turn to ensure accuracy. The front wall of the OWC is generally composed of a thin structure submerged in seawater, as shown in Fig. 3 (a). For the conventional fixed ghost particle method, the solid boundary representing the front wall is represented by ghost particles that each require an interpolation node at both sides. The particle on one side of the thin wall could be directly influenced by the particles on the other side (e.g., particle i and particle j). Six layers of ghost particles are required at the very least to avoid that influence. To achieve this, it could lead to a high particle resolution, which could be unnecessary for the rest of the fluid region, resulting in a high computational cost. Parallelization and a variable resolution model can reduce the computational cost, but would need significant changes to the SPH code structure. Additionally, multi-resolution SPH models suffer more difficulties for the regular particle distribution. Usually, irregular particle distribution may lead to the loss of numerical accuracy and tensile instability (Hu et al., 2017). In order to overcome this problem, a multi–node fixed ghost particle approach proposed by Meringolo et al. (2015) can be adopted to simulate the front wall. More interpolation nodes to a single fixed ghost particle are used to allow interaction with fluid particles located at different positions in the computational domain around the thin front wall, as shown in Fig. 3 (b). A fixed ghost particle may correspond to several interpolation nodes at different positions in the computational domain around the thin front wall. Thus, ghost particles have several different series of physical properties. When dealing with fluid particles, the properties of ghost particles are selected according to the fluid particle positions. Nevertheless, at least three layers of particles are still required by the multi–nodes fixed ghost particle method. The drawbacks of the conventional

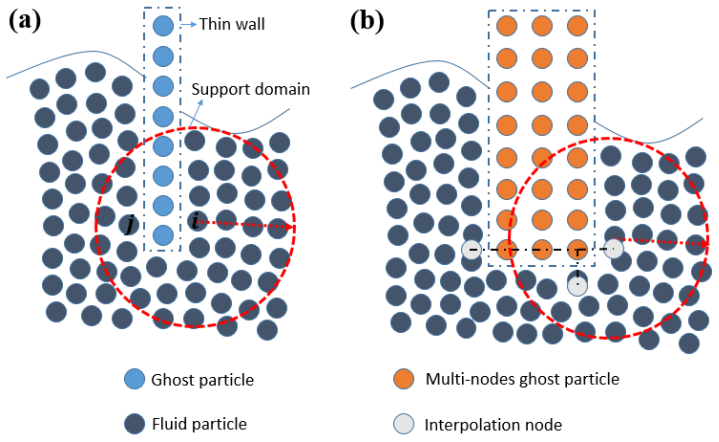

Figure 3: Sketch of the front wall (a) and multi-node ghost particle boundary (b).

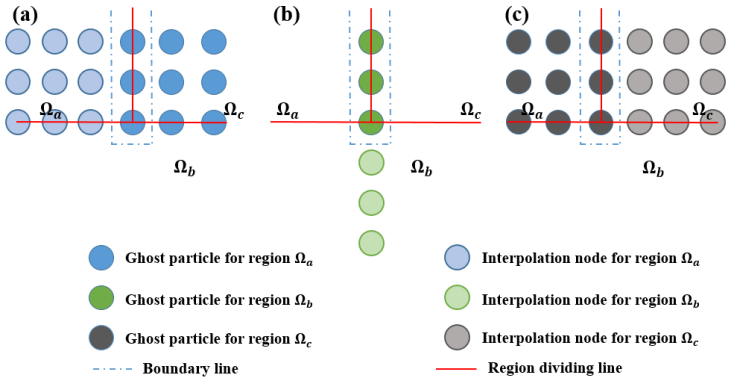

Figure 4: Regional dividing and ghost particle set up for fluid domain near a thin structure..

approach still arise when the front wall is too thin, i.e., the resolution is still strictly dependent on the thickness of the wall.

To break the dependence of particle resolution on the thickness of the front wall, regional ghost particles are used to define the thin front wall. The regional ghost particles can isolate the mutual influence of fluid particles and ghost particles from different sides of the thin wall. They can build a direct relationship between the fluid particles and the relative ghost particles in different regions.

2.4.1.1 Process of the regional ghost particle

The procedure of the application of regional ghost particles is illustrated as

follows:

1. Divide fluid field near the thin structure into three regions Ω_a, Ω_b and Ω_c according to the regional dividing line, as shown in Fig. 4. Set up regional ghost particles and the corresponding interpolation nodes for each region. The regional dividing line is the line used to divide the fluid region, while the boundary line is regarded as the wall boundary position, as shown in Fig. 3 and Fig. 4;

2. Determine the properties of ghost particles according to corresponding interpolation nodes. When calculating the interpolation node property, only the fluid particles in the related region are considered. For example, only the fluid particles in region Ω_a are used to calculate the properties of interpolation node for region Ω_a;

3. When calculating the fluid particles in region Ω_a, only the fluid particles in regions Ω_a, Ω_b and ghost particles for region Ω_a are taken into account. The same procedure can be easily adapted to the fluid particles in region Ω_c. When calculating fluid particles in region Ω_b, the fluid particles in regions Ω_a, Ω_b and Ω_c, and ghost particles for the region Ω_b are considered.

In the regional ghost particle approach, the fluid around the thin wall is divided into three regions. The fluid particles in region Ω_c have no influence on any particles in region Ω_a. The properties of the ghost particles for region Ω_a are calculated merely considering the fluid particles in the region Ω_a. That means the fluid on different sides of the thin wall have no direct hydrodynamic interaction, which is consistent with practice. The interpolation method follows the conventional fixed ghost method. In this way, the regional ghost particle approach can theoretically simulate thickness of the wall using lower resolution, and can overcome the limit of ghost particles for thin structures.

2.4.1.2 Discussion about regional dividing approaches

The approach to divide the regions is the key to the regional ghost particle approach. Here, three different approaches (see Fig. 5) are examined. Approach

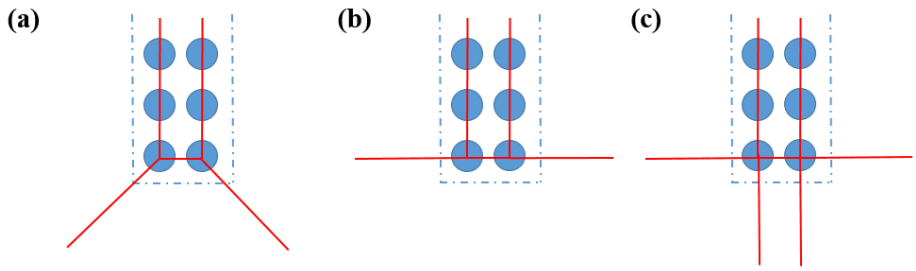

Figure 5: Different Regional dividing approaches for fluid domain around a thin structure..

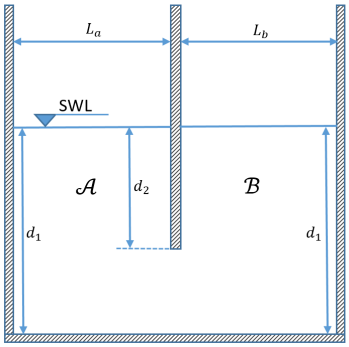

Figure 6: Schematic of the communicating vessel.

(a) is the same regional dividing approach proposed by Meringolo et al. (2015) for modelling wave–perforated breakwater interaction, except that here we define the regional dividing line at the location of ghost particles, rather than at the boundary line. In this way, the instability caused by particle proximity may be avoided. Approach (b) is another simple approach, which is similar to the method proposed in He et al. (2019b). For approach (c), the fluid is divided into five parts. However, the region at the bottom of the wall is narrow. In some cases, there could be very few particles. In extreme cases, it is possible that even no fluid particle may belong to this region. Also, having five regions results in a more complex code.

A communicating vessel is used as a case study to examine the performance of the regional ghost particle method using different region dividing approaches. The communicating vessel is composed of a pair of containers filled with a ho-

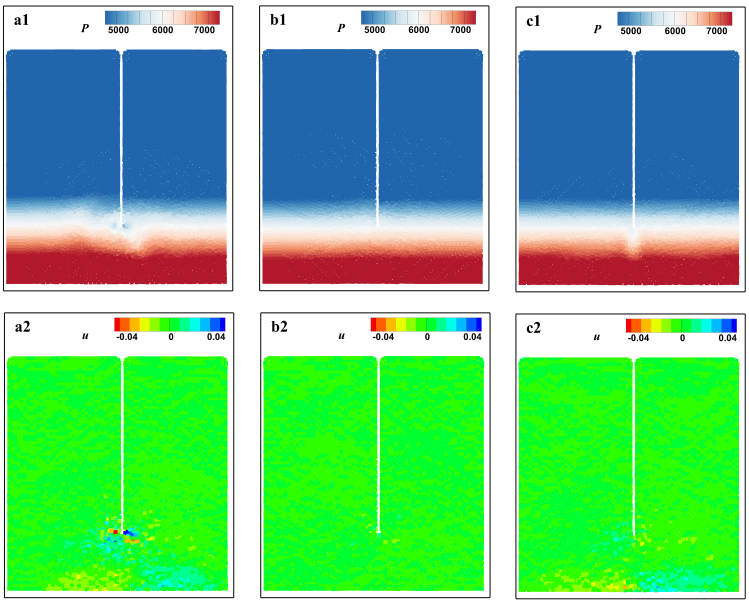

Figure 7: The hydrostatic pressure (a1∼c1) and horizontal velocity field (a2∼c2) of communicating vessel at t=10 s using approach (a) (a1, a2), approach (b) (b1, b2) and approach (c) (c1, c2).

mogeneous fluid, connected at the base, as shown in Fig. 6. The two containers $\mathcal{A}$ and $\mathcal{B}$ have slightly different widths $L_a = 0.35$ m and $L_b = 0.32$ m. The depth of the filled water is $d_1 = 0.8$ m, the submergence of the dividing wall in the middle is d_2 =0.6 m and its thickness is 0.01 m. Initially, the particle spacing is 0.01 m, i.e., the wall is modelled with one layer of ghost particles.

Fig. 7 presents the predicted pressure fields of the water in the communicating vessel at $t = 10.0$ s obtained by using three different regional dividing approaches. The main difference in the pressure field for different regional dividing approaches occurs at the bottom end of the thin wall. For approach (a), the pressure field at both sides of the wall, is not stable. This also influences other parts of the flow field, e.g., unstable pressure is also observed at the bottom of the vessel. As shown in Fig. 7, stability of the pressure field is achieved when using approach (b), however, it is underestimated by approach (c). Moreover,

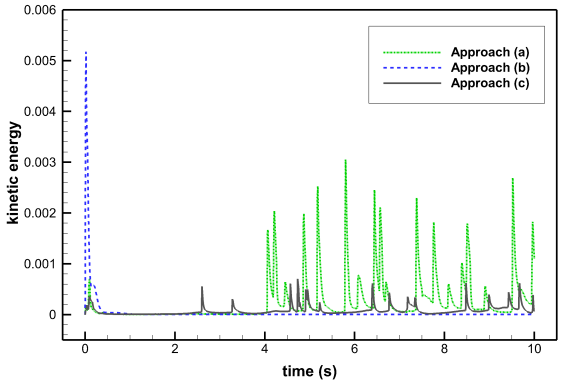

Figure 8: The time series of kinetic energy for the three approaches.

approach (b) achieves a more stable velocity field. After the initial oscillation, the water remains essentially static in approach (b) as shown by Fig. 8, which plots the variation of kinetic energy with time. Whereas, unstable states are observed for both approach (a) and approach (c). Thus, region dividing approach (b) is adopted hereinafter for the regional ghost boundary method for the rest of numerical simulations in this paper.

2.5. Wavemaker theory

Regular waves are produced by the piston–type wavemaker which is located at one end of the long water tank. The Biesel transfer functions express the relation between wave amplitude and wavemaker displacement, under the assumption of irrotational and incompressible flow and constant pressure at the free surface. For a piston–type wavemaker the Biesel transfer function Φ can be expressed as follows:

$$\Phi = \frac{H_{wave}}{S_0} = \frac{4\sinh^2(kd)}{2kd + \sinh(2kd)}, \tag{22}$$

where H_{wave}, S_0, k and d are the wave height, piston stroke, wave number and the water depth. Once the piston stroke is defined, the velocity $U(t)$ of piston movement is given by Wen et al. (2018):

$$U(t) = \frac{\mathrm{d}X(t)}{\mathrm{d}t} = \frac{\omega}{\Phi}(2\eta - \eta_{sph}), \tag{23}$$

where $X(t)$ is the position of the wavemaker movement. ω is the wave frequency. η is the local target water surface elevation and η_{sph} is the instantaneous water surface height at a measurement point $4h$ from the wavemaker. This distance (i.e., $4h$) is selected to ensure that the fluid particles used to measure free-surface elevation are not neighbours of the boundaries of the piston..The work of Ursell et al. (1960) provided experimental verification of the accuracy of the first–order wave generation theory for a piston–type wavemaker. The velocity of the wavemaker can be determined based on the far–field solution of the free surface elevation.

3. OWC hydrodynamic efficiency

The hydrodynamic efficiency of the OWC device is defined as the ratio between the time averaged–power absorbed by the OWC (P_{owc}) and the corresponding incident wave power (P_{inc}):

$$\xi = \frac{P_{owc}}{P_{inc}}. \tag{24}$$

For regular wave conditions with wave period T, P_{owc} can be expressed as the time–average of the product of the flow rate by the air pressure variation:

$$P_{owc} = \frac{1}{T}\int_{t_0}^{t_0+T} Q_t P_a \mathrm{d}t, \tag{25}$$

where t_0 is a time when the device has already reached a steady state of motion. Q_t is the airflow rate ($Q_t = w_c q_d$).

Based on linear wave theory, the average power per unit width in the incident plane progressive waves of small amplitude is expressed as follows (Zhang et al., 2012):

$$P_{inc} = \frac{1}{4} g \rho A_i^2 \frac{\omega}{k}\left(1 + \frac{2kd}{\sinh(2kd)}\right), \tag{26}$$

where A_i is the incident wave amplitude.

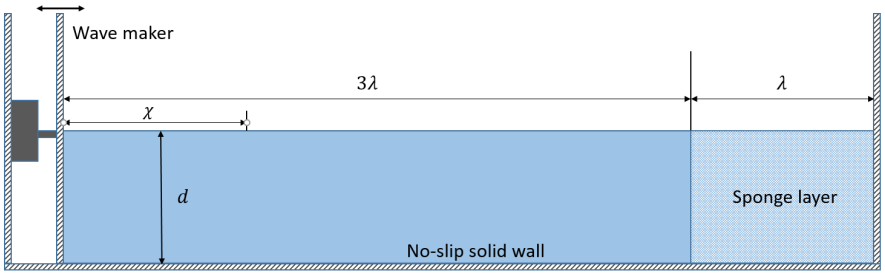

Figure 9: Sketch of a NWT.

4. Numerical validation

4.1. Wave propagation and convergence analysis

The first step towards the investigation of OWC is to develop a robust NWT. This section is to verify the performance of a SPH–based NWT by comparing the numerical results with the analytical ones. Fig. 9 shows the 2D NWT, in which d and $L = 4\lambda$ represent the water depth and the tank length, respectively, where λ denotes the incident wavelength. There is a sponge layer with the length of λ at the right end of the tank which is modeled to dissipate wave power. The incident wave height is denoted by H. A piston–type wavemaker located at the left boundary of the tank is used to generate waves. The solid walls of the tank are modelled using no–slip boundary conditions.

In the sponge layer, the velocity of the particles can be modified as,

$$u = u_0 \cdot f(x, \mathrm{d}t), \tag{27}$$

in which u and u_0 are the corrected particle velocity and the velocity of the particle; $f(x, \mathrm{d}t)$ is the reduction function introduced by Altomare et al. (2017) to reduce the velocity of the particles at each time step according to their location

$$f(x, \mathrm{d}t) = 1 - \mathrm{d}t \cdot 10\left(\frac{x - x_0}{x_1 - x_0}\right)^2, \tag{28}$$

where $\mathrm{d}t$ is the duration of the time step, x is the position of the particles, x_0 and x_1 are the starting and ending positions of the sponge layer, respectively. For

quantifying and better evaluating the comparison between the reference results, the mean average errors for amplitude MAE_a and phase MAE_p are used, which are calculated according to equations

$$MAE_a = \frac{1}{N_a} \sum \frac{|\eta_{extr}^{ref} - \eta_{extr}^{sph}|}{A}, \tag{29}$$

$$MAE_p = \frac{1}{N_a} \sum \frac{|t_{extr}^{ref} - t_{extr}^{sph}|}{T}, \tag{30}$$

where $extr$ refers to the local extrema, A to the wave amplitude, T to the wave period and N_a to the number of wave crest. ref and sph denote reference data (e.g., theory or experimental data) and SPH results, respectively. The NWT is tested by the generation of Stokes 2^{nd} waves with T= 1.2 s, H= 0.1 m and d= 0.5 m. Time series of the water surface elevation at χ=0.5λ (a), λ (b) and 2λ (c) predicted by the SPH NWT with three different resolutions, i.e., $dx0$= 0.005 m, 0.01 m and 0.02 m, together with the theoretical solutions, are illustrated in Fig. 10. The waves generated by the NWT are found to propagate steadily with satisfactory accuracy, except $dx0$=0.02 m. As shown in Fig. 10a, there are some small changes of the surface elevation between 4 s to 6 s for $dx0$= 0.02 m. This is due to the method used to determine the free surface position being more sensitive to isolated particles when the spacing between particles is larger. Numerical results for the two finer resolutions overlay one another and agree well with the analytical results, indicating that a convergent solution seems to be achieved with $dx0 \leq$0.01 m. It was found that the MAE_a are 5.9%, 6.1% and 5.6% for the resolution ($dx0$=0.01 m) at the position a, b and c.And MAE_p are 1.5%, 1.3% and 1.9%. It gives confidence in the present SPH NWT for generating and absorbing waves.

4.2. Communicating vessel with pneumatic model

In this section, a communicating vessel is simulated to validate the pneumatic model (Fig. 11). For this cases, the two interconnected containers are with the same width L_c=0.32 m. The initial same water depth in containers $\mathcal{A}$ and $\mathcal{B}$ is the same d_1=d_2=0.56 m, as shown in Fig. 11, without any air pressure

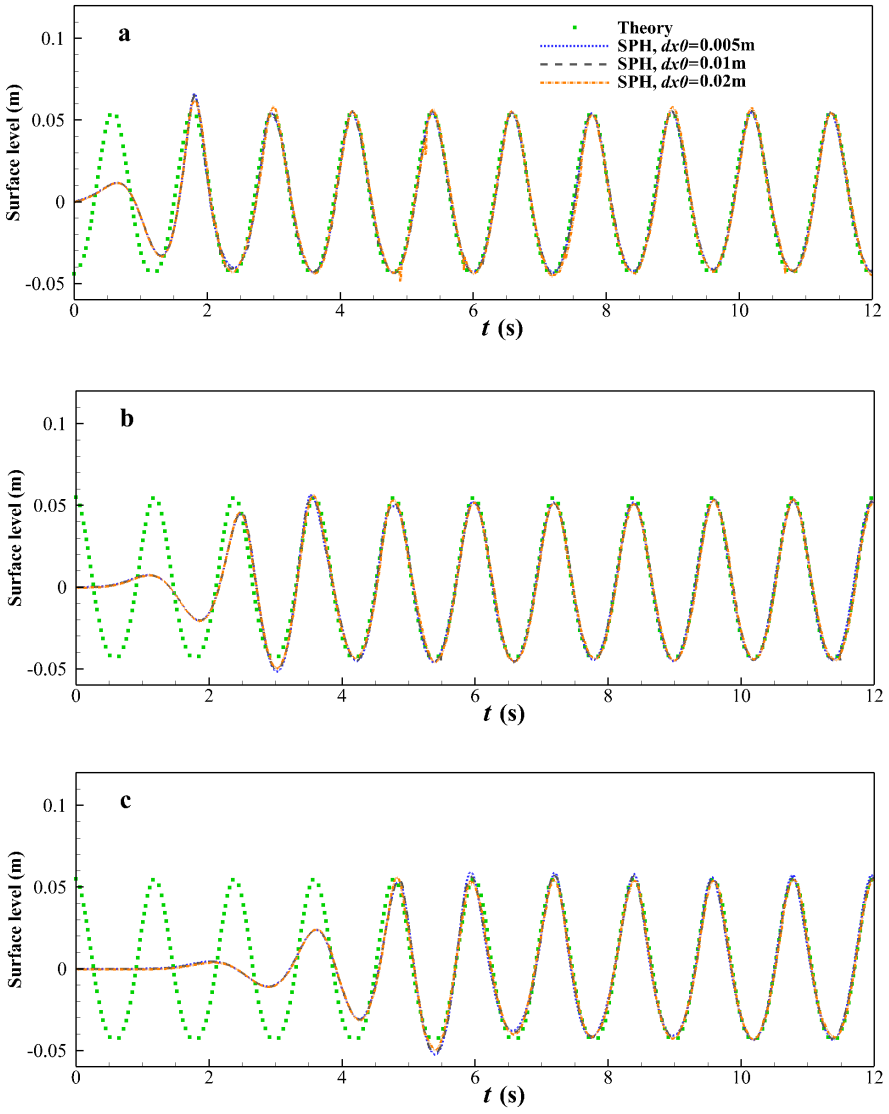

Figure 10: Time evolution of the surface elevation of a propagating Stokes 2^{nd} wave with T=1.2 s, λ=2.04 m and H=0.1 m at χ=0.5λ (a), λ (b) and 2λ (c).

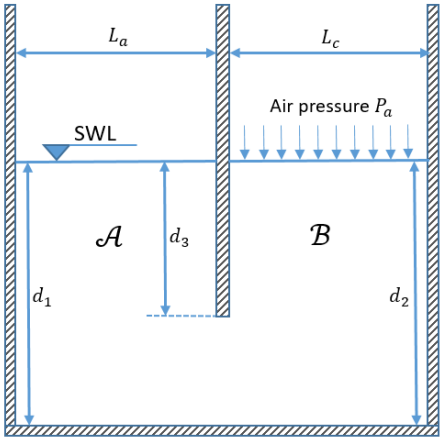

Figure 11: Sketch of the communicating vessel case.

imposed initially. The submergence d_3 and thickness of the connecting wall is 0.33 m and 0.01 m. Starting at t=0 s, the air pressure 1000 Pa is imposed in container $\mathcal{B}$. It means that the original level-balance will be broken, and the two enclosed water columns will oscillate up and down until a new balance is achieved, with a free surface level difference of H_d=1000/($g\rho$)=0.102 m.

Fig. 12 shows time series of significant difference for two particle resolutions. It can be seen that the free surface level difference oscillates with time and the amplitude of oscillation decays as time processes. Finally the free surface reaches a steady value (i.e., the theoretical solution), as expected. The predicted attenuation periods for dx0=0.01 m and 0.005 m coincide well with each other. Fig. 13 shows the pressure field at t=60 s with dx0=0.005 m. The free surface levels in containers $\mathcal{A}$ and $\mathcal{B}$ rise and fall, respectively, relative to the original situation. The pressure of the fluid at the free surface for containers $\mathcal{A}$ and $\mathcal{B}$ also changes and becomes the same value as the corresponding air pressure. Overall, it is demonstrated that the pneumatic model has been successfully integrated into the single-phase SPH model.

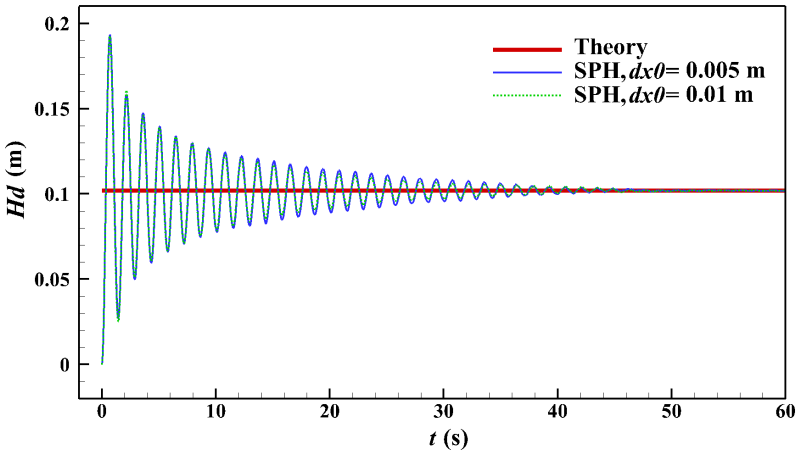

Figure 12: Time series of the free surface level difference between containers $\mathcal{A}$ and $\mathcal{B}$.

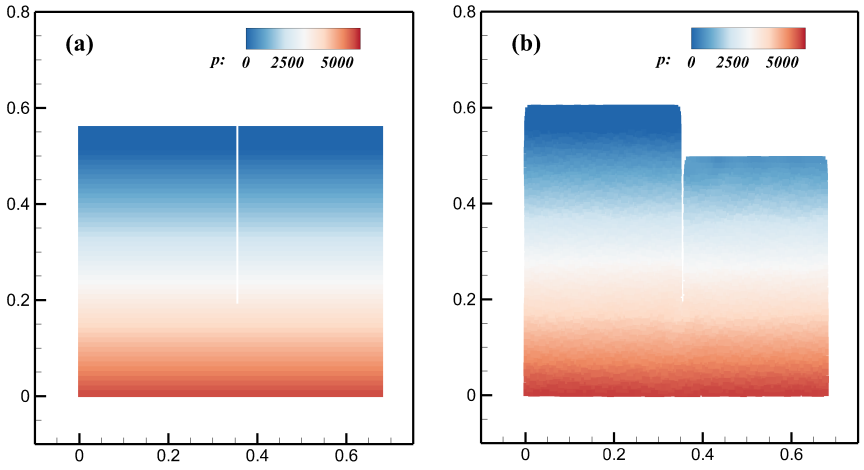

Figure 13: Snapshot of pressure field at t=0 s (a) and t=60 s (b) ($dx0$=0.005 m).

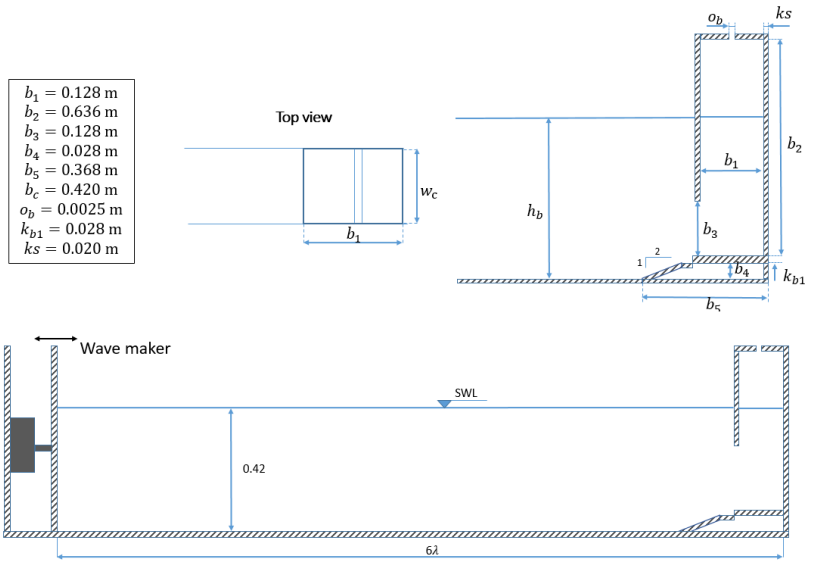

Figure 14: Schematic of the physical and the numerical water tank with OWC, dimensions in (m).

4.3. Numerical validation of an onshore OWC

In this subsection, an OWC with a platform at the bottom, as studied by López et al. (2014) is simulated (see Fig. 14). A slot, the 2D version of an orifice, is used to simulate the damping of the turbine. The air pressure and airflow rate through the turbine are considered to have a quadratic relationship Eq. (13) and can be used to assess air pressure (López et al., 2014). In López et al. (2014), a dimensionless coefficient B^* used to express the damping coefficient can be written as

$$B^* = \frac{|P_a|^{0.5}}{|q_d|} \frac{b_1}{\rho_{air}^{0.5}}, \tag{31}$$

where ρ_{air} is air density and b_1 is the chamber length. Combining Eq. (31) with Eq. (13), the damping coefficient K_{dm} can be calculated using

$$K_{dm} = \frac{B^* \rho_{air}^{0.5}}{b_1}. \tag{32}$$

According to López et al. (2014), B^*=63.45 is adopted for the 2.5 mm slot width. Thus, we can obtain K_{dm}=534.66 $\mathrm{kg}^{-0.5}\mathrm{m}^{-2.5}$.

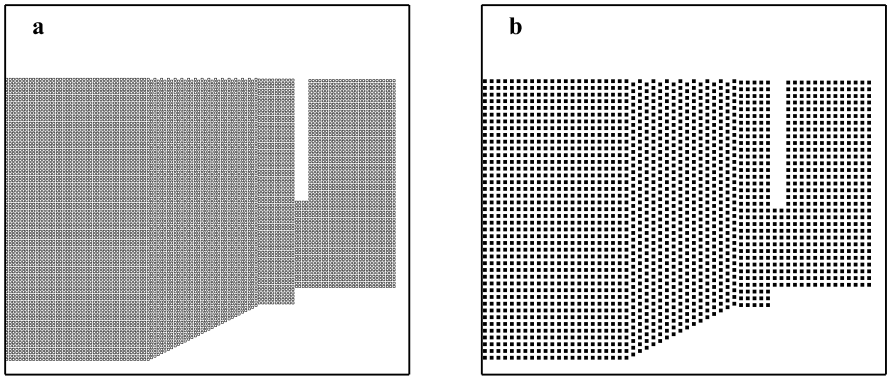

Figure 15: Initial particle arrangement at the vicinity of the OWC ((a): $dx0$=0.005 m, multi-node ghost particles approach; (b): $dx0$=0.01 m, regional ghost particle approach).

Table 1: SPH setup and computational time

Approach	Resolution (m)	Time step (s)	Physical time (s)	Calculation time (h)
Multi-node particle	0.005	0.00005	21	245.2
Regional ghost particle	0.01	0.0001	21	36.1

As shown in Fig. 15, the OWC has a thin front wall (k_s= 0.02 m). Since at least three layers of ghost particles are required for the multi–node ghost particles method, i.e., $dx0 \leq$0.007 m, here $dx0$=0.005 m is adopted as an initial particle resolution, leading to about 160000 particles for the whole field. Thanks to the present regional ghost particle method, which breaks the dependence of particle resolution on the thickness of the front wall, it now makes it possible to employ a larger value of $dx0$. Hence, $dx0$=0.01 m, i.e., two layers of ghost particles, can be taken as another initial particle resolution with the employment of the regional ghost particle method, resulting in approximately 40000 particles for the simulation. Regional ghost particles can reduce the number of particles required for the whole computational domain, and hence significantly reduce computational cost. One point should be noted that the converged results are achieved with these two particle resolutions, as shown in §4.1. The surface elevations and air pressure drop of the experimental data and the SPH results

with different resolutions are compared in Fig. 16. SPH with multi–node ghost particles ($dx0 = 0.005$ m) and SPH with regional ghost particles ($dx0 = 0.01$ m) show almost the same result and compare well with the experimental data, with almost same MAE_a of 7.2% (surface elevations, multi–node ghost particles) and 7.8% (surface elevations, regional ghost particles), with MAE_p of 3.7% (surface elevations, multi–node ghost particles) and 3.8% (surface elevations, regional ghost particles)in Table 2. The amplitude of the oscillation for the free surface evolution in the chamber are well captured. The initial computational setup and computational time for these two approaches are listed in Table 1. The simulations are performed on a desktop computer using an Intel(R) Core(TM) i5-7500T CPU Processor (Quad-Core, 2.71 GHz) under a WINDOWS 7 (64-Bit Edition) operating system. Less computational cost is required by the regional ghost particle method, indicating significant advantage of the regional ghost particle method.

Fig. 16 shows the SPH predicted time series data for the chamber differential air pressure and the chamber free surface elevation at its centre in comparison with experimental data (López et al., 2014) and CFD (Star–CCM+) results (Elhanafi et al., 2016). Validation of the wave generation at 6 wavelengths in front of the wavemaker can be seen in Appendix A. The surface–level results of SPH and Star–CCM+ both agree well with experimental data. For the pressure time series, Star–CCM+ results show a better fit than SPH results at some moments in time (t/T=12.8, 13.4, and 14.8). This may be due to the fact that both the air and water phases are simulated in the Star-CCM+ model, whereas only the water phase is modelled in the SPH model. In spite of this, the frequency and peak value of the SPH air pressure results are generally consistent with experimental data, with a MAE_a of only 8.8% and 8.1% and MAE_p of only 4.4% and 4.5% for multi–node ghost particles results and regional ghost particles results.

The present results, as shown in Fig. 17 agree well with the numerical CFD results by Elhanafi et al. (2016) despite some small discrepancies. To compare the time series of each parameter in wave periods on the same vertical axis scale,

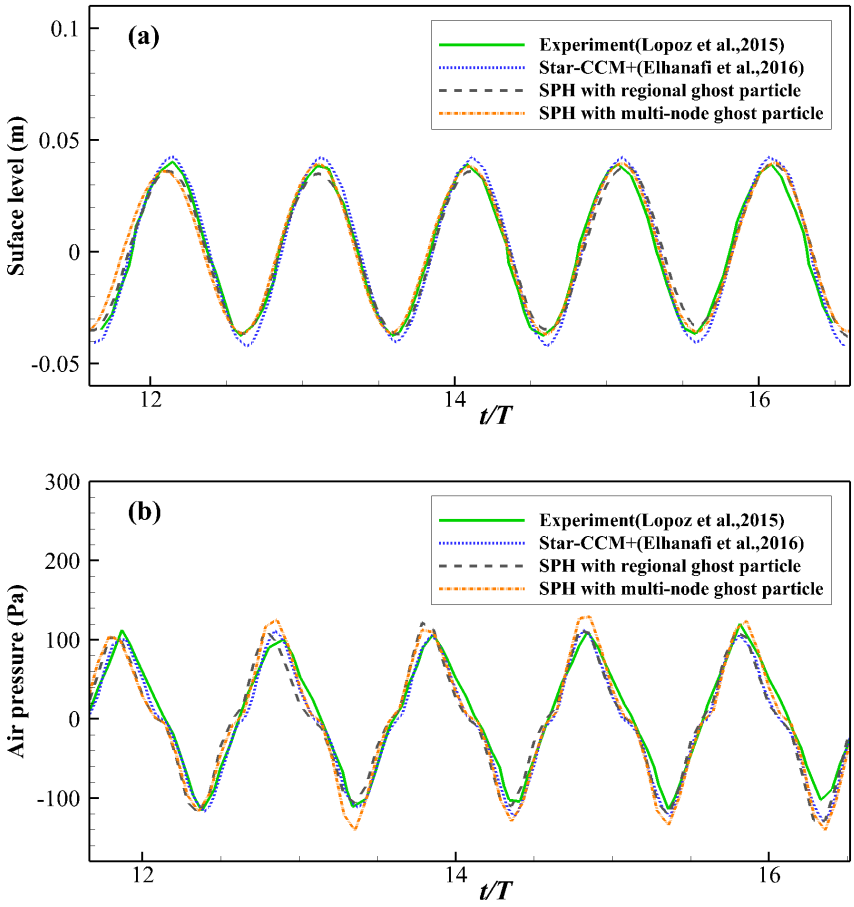

Figure 16: Comparison of relative free surface elevation (a) and air pressure drop (b) inside the chamber, for H=0.04 m, λ=2.42 m and T=1.4 s, with experimental data and CFD (Star-CCM+) numerical results.

Table 2: Errors in phase and amplitude for the numerical results

Approach	MAE_a (Surface evolution)	MAE_p (Surface evolution)	MAE_a (Air pressure)	MAE_p (Air pressure)
SPH with regional ghost particle	7.8%	3.8%	8.1%	4.5%
SPH with multi-node ghost particle	7.2%	3.7%	8.8%	4.4%

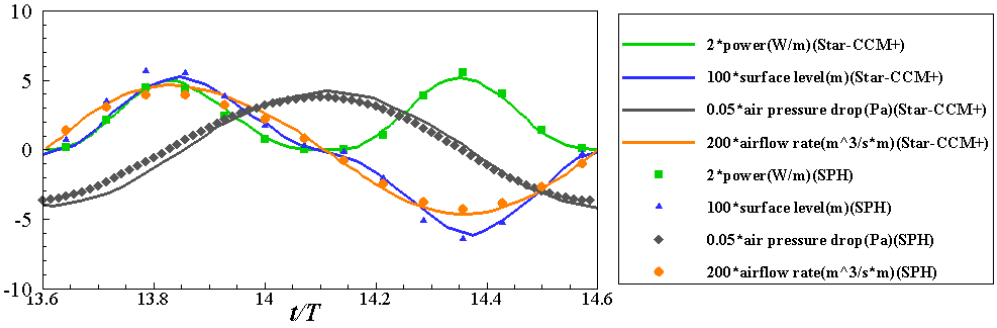

Figure 17: Free surface level inside the chamber, differential air pressure, air velocity, air volume flow rate, and power for H=0.04 m and T=1.4 s.

power, surface level, air pressure drop and air flow rate are multiplied by parameters (2, 100, 0.05 and 200). Starting where the water level inside the chamber is minimum (about t/T=13.60), the chamber free surface vertical velocity is almost zero due to the negligible gradient of the free surface time series. As time goes on, the water column inside the OWC chamber starts rising, both the rate of change in the chamber free surface and the velocity start to increase. The extracted power peaks almost when the water level reaches its initial still free surface level at about t/T=13.85. Further upward water movement results in increasing air velocity and pressure. The extracted power diminishes and returns to zero at about t/T=14.10, where the outflow stage switches into the inflow stage, and the water level begins to fall. Consequently, both the air velocity and pressure increase until approximately t/T=14.35 when the extracted power reaches its maximum. After that, the air velocity and the pressure decrease until they are approximately zero when the water column achieves its lowest level at about t/T=14.60. In this section, the free surface evolution is used to determine the air phase volume change. Then we use quadratic representation of Eq. (13) to calculate air pressure, and impose on the free surface inside the chamber. The time series of the predicted free surface level and air pressure agree well with the published experimental and numerical data (See Fig. 16), demonstrating that the quadratic representation of Eq. (13) works well in rep-

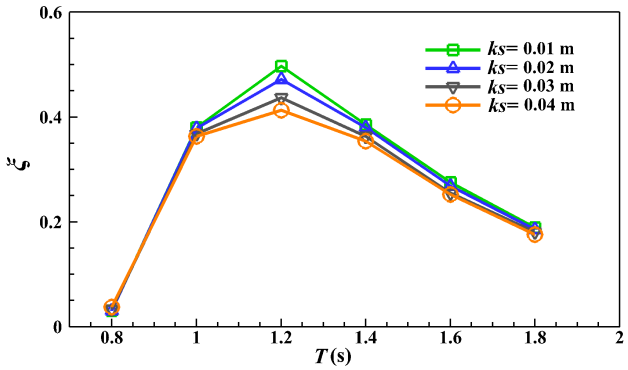

Figure 18: Comparison of hydrodynamic efficiency (ξ) for different thickness (ks) of front wall.

resenting the relationship between the air pressure inside the chamber and the air flux at the duct.

5. Performance analysis and discussion

In this section, the validated numerical model with the employment of the regional ghost particle method and $dx0$=0.01 m is applied to investigate the impact of front wall thickness, wave conditions in terms of wave height and wave period, together with the damping factors, on the hydrodynamic performance of the OWC as given in §4.3.

5.1. Effect of the wall thickness on the hydrodynamic performance

Performance of the OWCs with various front wall thickness (ks=0.01 m, 0.02 m, 0.03 m and 0.04 m) is examined in this subsection while keeping the same b_1 (The natural period of oscillation inside the OWC chamber depends on the value of b_1 (Zhang et al., 2012)). Six wave periods, T=0.8 s, 1.0 s, 1.2 s, 1.4 s, 1.6 s and 1.8 s are considered with the same damping factor K_{dm}=534.66 and the same wave height 0.04 m. Results for these 24 cases are illustrated in Fig. 18.

It is observed that an increase of the front wall thickness results in a lower hydrodynamic efficiency for all of the computed wave periods, expect T=0.8 s. This effect is most visible around T=1.2 s, where the peak of the hydrodynamic efficiency occurs. The efficiency ξ is found to decrease by about 3% for every 0.01 m increasement of the thickness at T=1.2 s. The effect of the front wall thickness becomes less obvious when the wave period is away from T=1.2 s. For example, the hydrodynamic efficiency ξ decreases by less than 1% for increasing 0.01 m thickness at T=1.4 s. It is noted that the wave period where the peak of hydrodynamic efficiency occurs is not sensitive to the change of the front wall thickness. The results illustrated in Fig. 18 demonstrate that the OWC with a thinner front wall can generally achieve a better performance in terms of wave power absorption within the range of wave conditions tested.

5.2. Effect of damping coefficient and wave height on the hydrodynamic performance

The parabolic expression Eq. (13) with the damping coefficient K_{dm} is used to simplify air–water phase model for the OWC to single–phase (water) model by assessing transient air pressure in the chamber. K_{dm} plays a significant role in influencing the performance of the pneumatic model and the hydrodynamic performance of the OWC as well. In order to investigate the effect of K_{dm}, the OWCs with seven dimensionless coefficients B^*=30.51, 67.37, 86.09, 121.96, 162.81, 197.62 and 263.20, which correspond with seven damping coefficients K_{dm}=257.09 $\mathrm{kg}^{-0.5}\mathrm{m}^{-2.5}$, 567.69 $\mathrm{kg}^{-0.5}\mathrm{m}^{-2.5}$, 725.44 $\mathrm{kg}^{-0.5}\mathrm{m}^{-2.5}$, 1027.70 $\mathrm{kg}^{-0.5}\mathrm{m}^{-2.5}$, 1371.92 $\mathrm{kg}^{-0.5}\mathrm{m}^{-2.5}$, 1665.25 $\mathrm{kg}^{-0.5}\mathrm{m}^{-2.5}$ and 2217.86 $\mathrm{kg}^{-0.5}\mathrm{m}^{-2.5}$, are selected as different cases to be studied. Different values of B^* correspond to different values of O_b (the slot width). Additionally, five wave heights, H^* ($H/b1$)=0.16, 0.31, 0.47, 0.63 and 0.78 are considered to test the effect of wave height on wave power absorption. The remaining parameters are the same to those adopted in the previous sections, e.g., water depth 0.42 m, wall thickness ks= 0.01 m and wave period T=1.2 s. Fig. 19 presents the contours of the hydrodynamic efficiency ξ against the dimensionless wave height

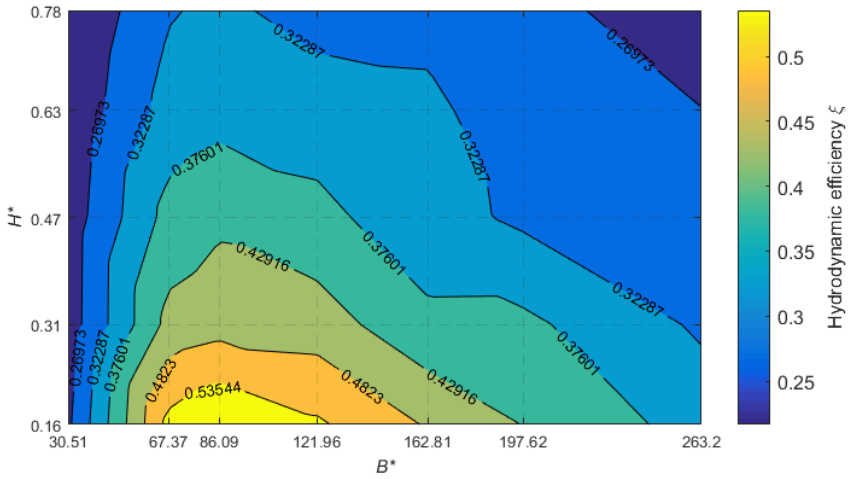

Figure 19: Variation of the hydrodynamic efficiency (ξ) with the dimensionless wave height (H^*) and different values of the damping coefficient (B^*) for wave period T=1.2 s.

(H^*) and the damping coefficient (B^*).

As expected, the hydrodynamic efficiency ξ is significantly affected by the damping coefficient. For any specified wave condition, there is a specific value of the damping coefficient to maximize the hydrodynamic efficiency of the OWC. The influence of the dimensionless wave height is also clear. Within the range of wave conditions tested, the higher values of the hydrodynamic efficiency are achieved for the smaller values of the dimensionless wave height. Taking the case with B^*=121.96 as an example, the hydrodynamic efficiency for the dimensionless wave height H^*=0.16 is 0.54, which is larger than the one (ξ=0.32) for H^*=0.78. This may result from a significant power dissipation due to vortex shedding and turbulence at the lip of the front wall in strong waves (Elhanafi et al., 2016). While, from the view of dimensional wave power absorption, the time averaged–power P_{owc} for H^*=0.16 is 0.30 W, which is much lower than the power P_{owc}=4.06 W for H^*=0.78 because of less incident wave power. Thus, the OWC might be preferable to work under high wave height conditions if the structural strength and device survivability can be ensured. There is no clear dependence between the dimensionless wave height and the optimal damping

coefficient. Despite the change in wave height, the maximum hydrodynamic efficiency remains around B^*=86.09 for the range of wave conditions tested.

A slot is usually regarded as a solution to emulate the behavior of an impulse turbine (Morris-Thomas et al., 2007). Different slots in the chamber results in the various damping coefficients (López et al., 2014). For a given wave condition, the value of the damping coefficient leading to the largest values of pneumatic power can be determined based on the present numerical model. Then the characteristics of the turbine can be determined to achieve the optimum coupling.

6. Conclusions

A single–phase SPH model with an integrated pneumatic model was used to simulate OWC wave energy devices with a PTO system in regular wave conditions. By employing a relationship between the air pressure and the air volume flux across the orifice, and neglecting the air compressibility, the air pressure inside the chamber is predicted based on the internal free surface–level changes. Meanwhile, the air pressure is introduced into the boundary conditions of the free surface inside the chamber to consider the influence of pneumatics on hydrodynamics. In order to simulate the thin front wall, the flow field near the front wall is divided into three different subdomains, where the fluid particles are associated with ghost particles for different regions. In this way, particle resolution can be independent of the thickness of the wall. Three case studies are used to validate the present SPH model, including a wave tank, a communicating vessel and simulations of OWC physical experiments. Once the model was validated, it was used to carry out an in–depth analysis of various wall thicknesses and the damping coefficient under various wave conditions. Finally, the following conclusions can be drawn:

- The present single–phase SPH–based NWT works well in wave generation and wave dissipation.

- Regional ghost particles can be used to simulate the thin front wall. This gives great flexibility of the choice of initial particle spacing, and so sim-

ulations can be carried out with fewer particles than using multi–node ghost particles.

- The present single–phase SPH model with a parabolic expression including the damping coefficient can be used as a practical tool for capturing the free surface elevation, air pressure, and evaluating wave power absorption of the OWC.

- Within the range of wave conditions tested and the front wall thickness, the OWC platform with thinner walls has a better performance in terms of hydrodynamic efficiency.

- Within the range of wave conditions tested, the higher values of the hydrodynamic efficiency are achieved for the smaller values of the dimensionless wave height.

- There is a specific value of the damping coefficient that maximizes the hydrodynamic efficiency for a given wave condition. The optimal damping coefficient is not sensitive to the change of the dimensionless wave height.

This work shows the capability of SPH for simulating an OWC and PTO system. Although the two–phase SPH model can predict airflow near the orifice and simulate pneumatic conversion in a straightforward way, the expensive computational cost makes it prohibitive. This article offers one possible solution, which is to simulate OWC with PTO using a single–phase model. It can be used in the preliminary stage of the device design and preliminary selection of turbine performance, allowing to comparatively test a considerable number of design alternatives with reduced computational effort. In the future, we will consider the irregular wave conditions, and extend the SPH model for floating OWCs. When applying the pneumatic conversion to moving OWCs, the approach for measuring air volume needs to be adjusted more or less to consider the effect of the moving structures. Meanwhile the mooring system also needs to be developed.

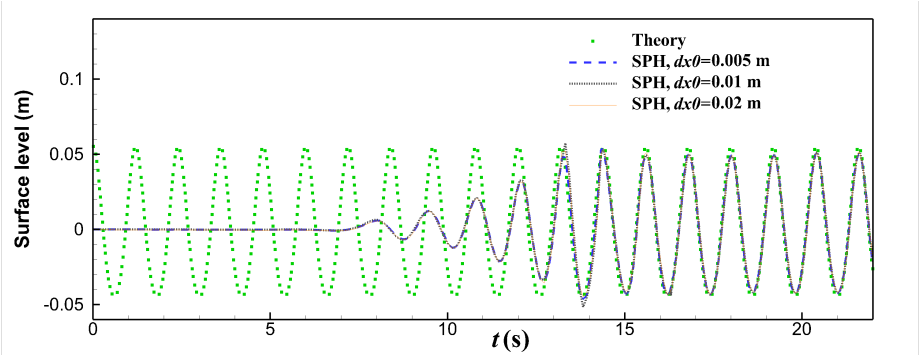

Figure A.20: Time evolution of the surface elevation of a propagating wave with T=1.2 s, λ=2.04 m and H=0.1 m at 6 wavelengths in front of the wavemaker.

Acknowledgements

The research was supported by the financial support from China Scholarship Council (Grant No. 201806060137). The corresponding author gratefully acknowledges the support from Intelligent Community Energy (ICE), INTERREG V FCE, European Commission (Contract No. 5025), and Open Research Fund Program of State Key Laboratory of Ocean Engineering, Shanghai Jiao Tong University (Grant No. 1916).

Appendix A. Validation of the wave generation

To compare wave propagation at 6 wavelengths in an empty NWT, we extended the tank in §4.3 to 8 wavelengths with one wavelength sponge layer at the right end of the tank. The numerical prediction for the wave time-series at a distance of 6 wavelengths from the wave maker is plotted alongside the theoretical results in Fig. A.20. It can be seen that the numerical results are in excellent agreement with the theoretical values, with MAE_p 6.3% and MAE_p 1.8% for resolution 0.01 m.

References

Altomare, C., Domínguez, J.M., Crespo, A.J.C., González-Cao, J., Suzuki, T., Gómez-Gesteira, M., Troch, P., 2017. Long-crested wave generation and absorption for SPH–based DualSPHysics model. Coastal Engineering 127, 37–54.

Antuono, M., Colagrossi, A., Marrone, S., 2012. Numerical diffusive terms in weakly–compressible SPH schemes. Computer Physics Communications 183, 2570–2580.

Antuono, M., Colagrossi, A., Marrone, S., Lugni, C., 2011. Propagation of gravity waves through an sph scheme with numerical diffusive terms. Computer Physics Communications 182, 866–877.

Brito, M., Canelas, R., García-Feal, O., Domínguez, J., Crespo, A., Ferreira, R., Neves, M., Teixeira, L., 2020. A numerical tool for modelling oscillating wave surge converter with nonlinear mechanical constraints. Renewable Energy 146, 2024–2043.

Colagrossi, A., Landrini, M., 2003. Numerical simulation of interfacial flows by smoothed particle hydrodynamics. Journal of computational physics 191, 448–475.

Crespo, A.J.C., Altomare, C., Domínguez, J.M., González-Cao, J., Gómez-Gesteira, M., 2017. Towards simulating floating offshore oscillating water column converters with smoothed particle hydrodynamics. Coastal Engineering 126, 11–26.

Deng, Z., Wang, L., Zhao, X., Wang, P., 2020. Wave power extraction by a nearshore oscillating water column converter with a surging lip–wall. Renewable Energy 146, 662–674.

Didier, E., Neves, D.R.C.B., Teixeira, P.R.F., Dias, J., Neves, M.G., 2016. Smoothed particle hydrodynamics numerical model for modeling an oscillating water chamber. Ocean Engineering 123, 397–410.

Drew, B., Plummer, A.R., Sahinkaya, M.N., 2009. A review of wave energy converter technology. Proceedings of the Institution of Mechanical Engineers, Part A: Journal of Power and Energy 223, 887–902.

Elhanafi, A., Fleming, A., Macfarlane, G., Leong, Z., 2016. Numerical energy balance analysis for an onshore oscillating water column–wave energy converter. Energy 116, 539–557.

Elhanafi, A., Kim, C.J., 2018. Experimental and numerical investigation on wave height and power take–off damping effects on the hydrodynamic performance of an offshore–stationary OWC wave energy converter. Renewable Energy 125, 518–528.

Elhanafi, A., Macfarlane, G., Fleming, A., Leong, Z., 2017. Scaling and air compressibility effects on a three–dimensional offshore stationary OWC wave energy converter. Applied Energy 189, 1–20.

Evans, D.V., 1978. The oscillating water column wave–energy device. IMA Journal of Applied Mathematics 22, 423–433.

Evans, D.V., Porter, R., 1995. Hydrodynamic characteristics of an oscillating water column device. Applied Ocean Research 17, 155–164.

Falcão, A.F.d.O., Henriques, J.C.C., 2016. Oscillating–water–column wave energy converters and air turbines: A review. Renewable Energy 85, 1391–1424.

Gong, K., Shao, S., Liu, H., Wang, B., Tan, S.K., 2016. Two–phase SPH simulation of fluid–structure interactions. Journal of Fluids and Structures 65, 155–179.

Gotoh, H., Khayyer, A., 2018. On the state-of-the-art of particle methods for coastal and ocean engineering. Coastal Engineering Journal 60, 79–103.

He, F., Zhang, H., Huang, C., Liu, M., 2020. Numerical investigation of the solitary wave breaking over a slope by using the finite particle method. Coastal Engineering 156, 103617.

He, F., Zhang, H., Zhao, J., Zheng, S., Iglesias, G., 2019a. Hydrodynamic performance of a pile-supported OWC breakwater: An analytical study. Applied Ocean Research 88, 326–340.

He, M., Gao, X., Xu, W., Ren, B., Wang, H., 2019b. Potential application of submerged horizontal plate as a wave energy breakwater: A 2D study using the WCSPH method. Ocean Engineering 185, 27–46.

Hu, W., Pan, W., Rakhsha, M., Tian, Q., Hu, H., Negrut, D., 2017. A consistent multi–resolution smoothed particle hydrodynamics method. Computer Methods in Applied Mechanics and Engineering 324, 278–299.

Huang, C., Zhang, D., Shi, Y., Si, Y., Huang, B., 2018a. Coupled finite particle method with a modified particle shifting technology. International Journal for Numerical Methods in Engineering 113, 179–207.

Huang, C., Zhang, D., Si, Y., Shi, Y., Lin, Y., 2018b. Coupled finite particle method for simulations of wave and structure interaction. Coastal Engineering 140, 147–160.

Kamath, A., Bihs, H., ∅. A. Arntsen, 2015. Numerical investigations of the hydrodynamics of an oscillating water column device. Ocean Engineering 102, 40–50.

Lee, E.S., Moulinec, C., Xu, R., Violeau, D., Laurence, D., Stansby, P., 2008. Comparisons of weakly compressible and truly incompressible algorithms for the SPH mesh free particle method. Journal of Computational Physics 227, 8417–8436.

Liu, M., Zhang, Z., 2019. Smoothed particle hydrodynamics (SPH) for modeling fluid–structure interactions. Science China Physics, Mechanics and Astronomy 62, 984701.

Liu, M.B., Liu, G.R., 2010. Smoothed particle hydrodynamics (SPH): an overview and recent developments. Archives of Computational Methods in Engineering 17, 25–76.

Liu, Z., Wang, Y., Hua, X., 2020. Numerical studies and proposal of design equations on cylindrical oscillating wave surge converters under regular waves using sph. Energy Conversion and Management 203, 112242.

López, I., Pereiras, B., Castro, F., Iglesias, G., 2014. Optimisation of turbine-induced damping for an OWC wave energy converter using a RANS–VOF numerical model. Applied Energy 127, 105–114.

Madhi, F., Yeung, R.W., 2018. On survivability of asymmetric wave-energy converters in extreme waves. Renewable Energy 119, 891–909.

Marrone, S., Antuono, M., Colagrossi, A., Colicchio, G., Touzé, D.L., Graziani, G., 2011. δ–SPH model for simulating violent impact flows. Computer Methods in Applied Mechanics and Engineering 200, 1526–1542.

Martins-rivas, H., Mei, C.C., 2009a. Wave power extraction from an oscillating water column along a straight coast. Ocean Engineering 36, 426–433.

Martins-rivas, H., Mei, C.C., 2009b. Wave power extraction from an oscillating water column at the tip of a breakwater. Journal of Fluid Mechanics 626, 395–414.

Meringolo, D.D., Aristodemo, F., Veltri, P., 2015. SPH numerical modeling of wave–perforated breakwater interaction. Coastal Engineering 101, 48 – 68.

Monaghan, J.J., 1989. On the problem of penetration in particle methods. Journal of Computational Physics 82, 1–15.

Monaghan, J.J., 1994. Simulating free surface flows with SPH. Journal of Computational Physics 110, 399–406.

Monaghan, J.J., 2005. Smoothed particle hydrodynamics. Reports on Progress in Physics 68, 1703–1759.

Morris, J.P., Fox, P.J., Zhu, Y., 1997. Modeling low Reynolds number incompressible flows using SPH. Journal of Computational Physics 136, 214–226.

Morris-Thomas, M.T., Irvin, R.J., Thiagarajan, K.P., 2007. An investigation into the hydrodynamic efficiency of an oscillating water column. Journal of Offshore Mechanics and Arctic Engineering 129, 273–278.

Nader, J.R., Zhu, S.P., Cooper, P., 2014. Hydrodynamic and energetic properties of a finite array of fixed oscillating water column wave energy converters. Ocean Engineering 88, 131–148.

Ning, D., Wang, R., Zhang, C., 2017. Numerical simulation of a dual–chamber oscillating water column wave energy converter. Sustainability 9, 1599.

Sarmento, A.J.N.A., Falcão, A.F.d.O., 1985. Wave generation by an oscillating surface–pressure and its application in wave–energy extraction. Journal of Fluid Mechanics 150, 467–485.

Simonetti, I., Cappietti, L., Elsafti, H., Oumeraci, H., 2017. Optimization of the geometry and the turbine induced damping for fixed detached and asymmetric OWC devices: A numerical study. Energy 139, 1197–1209.

Simonetti, I., Cappietti, L., Elsafti, H., Oumeraci, H., 2018. Evaluation of air compressibility effects on the performance of fixed OWC wave energy converters using CFD modelling. Renewable Energy 119, 741–753.

Sun, P., Zhang, A.M., Marrone, S., Ming, F., 2018. An accurate and efficient sph modeling of the water entry of circular cylinder. Applied Ocean Research 72, 60–75.

Ursell, F., Dean, R.G., Yu, Y.S., 1960. Forced small–amplitude water waves: a comparison of theory and experiment. Journal of Fluid Mechanics 7, 33–52.

Violeau, D., Rogers, B.D., 2016. Smoothed particle hydrodynamics (sph) for free-surface flows: past, present and future. Journal of Hydraulic Research 54, 1–26.

Vyzikas, T., Deshoulières, S., Giroux, O., Barton, M., Greaves, D., 2017. Numerical study of fixed oscillating water column with RANS–type two–phase CFD model. Renewable Energy 102, 294–305.

Wen, H., Ren, B., Yu, X., 2018. An improved SPH model for turbulent hydrodynamics of a 2D oscillating water chamber. Ocean Engineering 150, 152–166.

Ye, T., Pan, D., Huang, C., Liu, M., 2019. Smoothed particle hydrodynamics (sph) for complex fluid flows: Recent developments in methodology and applications. Physics of Fluids 31, 011301.

Zhang, D., Shi, Y., Huang, C., Si, Y., Huang, B., Li, W., 2018. Sph method with applications of oscillating wave surge converter. Ocean Engineering 152, 273–285.

Zhang, D., Shi, Y., Huang, C., Si, Y., Li, W., 2019. A mixed characteristic boundary condition for simulating viscous incompressible fluid flows around a hydrofoil. Journal of Marine Science and Technology 24, 73–85.

Zhang, Y., Zou, Q.P., Greaves, D., 2012. Air–water two-phase flow modelling of hydrodynamic performance of an oscillating water column device. Renewable Energy 41, 159–170.

Zheng, S., Antonini, A., Zhang, Y., Greaves, D., Miles, J., Iglesias, G., 2019a. Wave power extraction from multiple oscillating water columns along a straight coast. Journal of Fluid Mechanics 878, 445–480.

Zheng, S., Zhang, Y., Iglesias, G., 2019b. Coast/breakwater–integrated OWC: A theoretical model. Marine Structures 66, 121–135.